Materials & Design 241 (2024) 112958

Contents lists available at ScienceDirect

Materials & Design

journal homepage: www.elsevier.com/locate/matdes

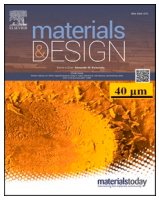

Experimental and theoretical investigation of failure mechanism in Al_2O_3/SiC composite under plane shock waves

Yubo Gao [a,b,*], Zhihao Li [a], Yanxin Ge [c], Liutong Shi [a]

[a] School of Aerospace Engineering, North University of China, Shanxi, Taiyuan 030051, China
[b] School of Mechanical and Aerospace Engineering, Nanyang Technological University, 50 Nanyang Avenue, 639798, Singapore
[c] State Key Laboratory of Explosion Science and Technology, Beijing Institute of Technology, Beijing 100081, China

ARTICLE INFO

Keywords:
Al_2O_3/SiC
Dynamic strength
Fracture mechanism
Fragments scale

ABSTRACT

The investigation of fracture and fragmentation is essential for evaluating the protection performance and structural design of ceramic armour. This paper focused on the dynamic failure and fracture mechanisms of the fine-grained Al_2O_3/SiC composite subjected to plane shock waves. The macroscopic shock response characteristic was determined through a series of plane impact tests, which included the Hugoniot curves of the composite. The results indicated that the fracture mechanism is significantly influenced by specific stress characteristics. The transgranular fracture in large grains and intergranular fracture in small grains exhibit obvious local plastic deformation characteristics. Moreover, the presence of second-phase SiC particles markedly influences both crack propagation and the microfracture mode of the composite. Lastly, a statistical analysis of the ceramic fragments was conducted after the soft recovery of specimens in impact experiments, and analytical models were developed and modified to predict the distribution of fragments under plane shock loading.

1. Introduction

In the past decades, ceramic materials have been increasingly utilized in protective structures of the lightweight armor system due to their higher hardness, greater strength, and lower density compared to metal materials [1,2]. Research has demonstrated that a typical penetration event can be divided into four distinct zones [3], as shown in Fig. 1.

In Zone I, the ceramic material preceding the penetrator remains largely intact. Underneath the penetrator in Zone II, the fractured ceramic is heavily interlocked by highly compressed and lateral restraint. Moving into Zone III, the predominant state is powdered material, with particles initiating a flow away from the target face as confinement is gradually relaxed [4]. Outside the comminuted zones is Zone IV, and cone, radial and lateral cracks exist in this range. So, the morphological characteristics of the damaged ceramic target is the key factor in its ballistic performance. Therefore, the morphological characteristics of the damaged ceramic target play a pivotal role in its ballistic performance. But until now, the dynamic failure and fracture mechanisms of ceramic materials remain insufficiently characterized and understood due to their typical traits of high compressive strength, low tensile strength, and low failure strain as brittle materials. To evaluate protection performance and further enhancing the structural design of ceramic composite armor, it is necessary to investigate the microscopic fracture mechanism and distribution and prediction of fragments sizes at the macroscopic scale [5,6].

The impact resistance of ceramic armor is significantly influenced by the dynamic fracture mode [7]. The research revealed that the propagation of cracks and the characteristics of fractured ceramic fragments change with varying loading rates [8–10]. At a macroscopic scale, the size of granular ceramics in the penetration zone increased with higher impact velocities, exhibiting distinct shapes [11]. Recently, more and more theoretical models have been developed and refined to predict the distribution of fragment sizes. Denoual et al. [12] proposed a damage model to address ceramics under dynamic loadings. Shenoy et al. [13] introduced a one-dimensional micromechanics-based statistical model for fragmentation in a brittle material, providing an accurate description of damage evolution during the crushing process. And the predicted fragment sizes showed good agreement with numerical results. Grady [14,15], based on energy conservation theory, established a classical theoretical model for brittle materials under dynamic fracture conditions, verified through experiments. Drugan [16] established a mechanics-based model predicting fragment size and time to fragmentation onset in terms of fundamental material properties and applied

* Corresponding author at: School of Science, North University of China, Shanxi, Taiyuan 030051, China.
E-mail address: gaoyb@nuc.edu.cn (Y. Gao).

https://doi.org/10.1016/j.matdes.2024.112958
Received 24 November 2023; Received in revised form 12 April 2024; Accepted 17 April 2024
Available online 18 April 2024

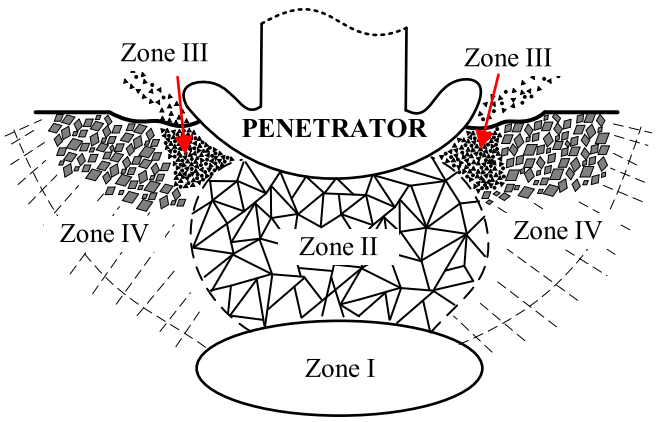

Fig. 1. Damage modes of ceramic target under high-velocity penetrator [3]: Zone I-highly-compressed sub-surface damage zone; Zone II-highly interlocked comminuted zone; Zone III-powdered comminuted zone; Zone IV-macro-cracked zone.

strain rate. This model considers the actual time-varying dynamic deformation occurring prior to fragmentation onset. Zhou et al. [17,18] presented a closed-form solution, specifically the dynamics of an isolated decohesion (DID) model, estimating fragment size in brittle materials under one-dimensional stress wave loading. The results showed reasonable predictions compared to the experimental data. Zhang et al. [19] proposed an analytical approach to estimate fragment flying speed and average fragment size based on strain energies and tensile properties of tested materials. In conclusion, existing research on the dynamic failure and fracture mechanisms of ceramics has predominantly concentrated on the one-dimensional stress wave loading condition, neglecting the consideration of planar shock wave loading with higher strain rates.

On the microscopic scale, the deformation and displacement of grains play a crucial role in determining the strength of brittle materials [20]. While macroscopic fracture of ceramic materials typically exhibits brittle failure under dynamic loading, a closer observation at the microstructure reveals the existence of local plastic deformation. For instance, polycrystalline AlN ceramics display plastic deformation characteristics, with an increase in transgranular fracture observed at higher strain rates [21]. Bhattacharya et al. [22] conducted dynamic compression experiments on coarse-grain alumina, revealing the formation of micro-cracks, shear bands, nanoscale cleavages, and dislocations. The occurrence of these features heightened with the strain rate. Until now, numerous researchers have observed that grain deformation in ceramic materials under dynamic loads can lead to the nucleation of microcrack tips, as well as the manifestation of dislocation and plastic deformation characteristics under localized shear forces [23,24].

This study focuses on the fine-grained Al_2O_3/SiC composite which has better mechanical properties compared to pure alumina (Al_2O_3). Previous research indicates that the incorporation of a second reinforced phase can enhance the strength and failure properties of ceramic composites by altering the generation, propagation, and interaction of microcracks [25–28]. Shi et al. [29] investigated the mechanical behaviors of Al_2O_3-nano SiC composite sintered by hot pressing. The results showed a significant improvement in fracture toughness and strength compared to monolithic Al_2O_3. The presence of SiC-reinforced particles enhanced the propagation resistance of microcracks within the matrix grains. Additionally, Gevorkyan et al. [30] observed an increase in the strength and wear resistance of alumina ceramics with the addition of SiC particles, along with a noticeable reduction in matrix material porosity. Until now, research on the Al_2O_3/SiC composite has primarily focused on microstructure, hardness, fracture toughness, flexural strength, and elastic modulus [30–34]. However, there is limited exploration of the dynamic mechanical properties and failure mechanisms of the composite despite their crucial importance for various applications in mechanical engineering and structural engineering [2].

In the present study, the dynamic mechanical behavior of the Al_2O_3/SiC composite was examined through a plane impact test. The SEM techniques were employed to obtain the failure and fracture mechanisms of the recovered fragments. A statistical analysis of the ceramic fragments was conducted after the soft recovery of specimens in experiments, and an analytical model was developed and modified to predict the distribution of fragments under plane shock waves.

2. Material and methods

2.1. Description of the Al_2O_3/SiC composite

In this study, the Al_2O_3/SiC composite contains the second reinforced phase of SiC powders with a content of 5 wt%. The composite has a density of 3670 kg/m^3. Fig. 2 shows the SEM morphology and elemental distribution of the composite. The maximum and minimum grain sizes were measured at 21.46 μm and 1.67 μm, respectively. The average size of Al_2O_3 grain followed a normal distribution, approximately 7.56 ± 0.08 μm, exhibiting the characteristic features of an α-sintered body. The SiC particles are distributed not only along the grain boundaries of the matrix Al_2O_3 but also within the interior of the grains. The matrix has been refined through the addition of the SiC phase. A few micro-pores are randomly distributed on the surface, and areas without pores show tight connections without obvious gaps.

To determine the basic mechanical properties of the Al_2O_3/SiC composite, dynamic compression tests were conducted using an improved split Hopkinson pressure bar. The cylindrical specimen has a diameter of 5.5 mm, and a length of 11 mm. The incident wave was modulated into a triangular pulse using a copper pulse shaper. The specimen underwent a constant strain-rate loading, as shown in Fig. 3 (a). The stress–strain curve exhibited linearly elastic behavior before failure, as shown in Fig. 3(b). The deformation of the composite showed a typical brittle characteristic, remaining in the elastic stage before failure. The compressive strength of the composite increased from 3.25GPa to 3.58GPa with the increasing of strain rates. Due to the small deformation of ceramics and the addition of inserts at both ends of the specimen, the compression strain measurement is inaccurate, making it impossible to obtain an accurate elastic modulus.

2.2. Experiment setup

In this study, the one-stage gas gun technology was utilized in the flyer plate impact tests. The apparatus consisted primarily of a high-pressure chamber and a launch tube with a 50 mm diameter. The experimental device was designed to facilitate the soft recovery of samples after impact tests, as shown in Fig. 4. The sabot included an aluminum alloy support and an adiabatic foam plastic support. The aluminum alloy support provided inertial acceleration to the sabot. The foam plastic support can reduce the mass of the sabot, and improve the air-tight property by continuous compression in high velocity motion, ensuring the proper motion attitude of the flyer. Both flyers and samples utilized the Al_2O_3/SiC composite to achieve symmetrical impact in a series of tests. The impact velocity can be measured using the on–off signals of two fine copper wires. The soft recovery system comprised two components: an inner tube and energy-absorbing foam. The inner tube primarily served as the initial support for the sample. When the ceramic sample broke under high-pressure impact, the damaged fragments moved along the inner tube. The kinetic energy of these fragments could then be absorbed by the adiabatic foam plastic, minimizing secondary fragmentation to the greatest extent possible.

The specimen was configured with three layers of ceramic plates, each having a thickness of 2 mm and a diameter of 20 mm. Epoxy resin was employed to bond the ceramic plates and sensors, with a curing time

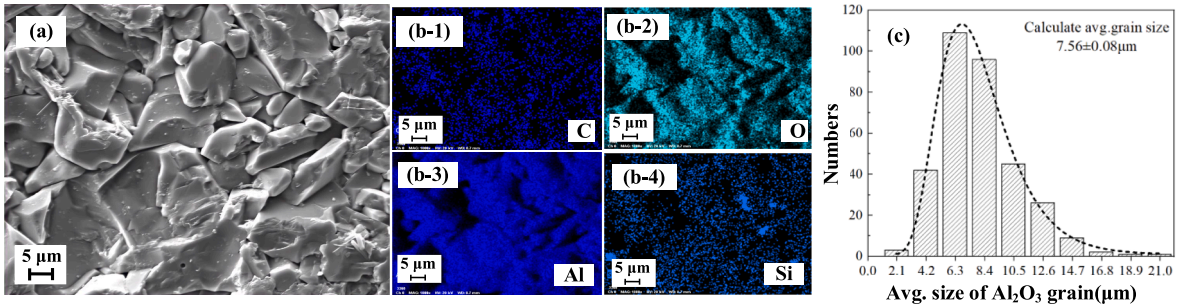

Fig. 2. Microstructure of the Al_2O_3/SiC composite. (a) SEM morphology of fracture surface; (b) Elemental distribution: (b-1) Carbon, (b-2) Oxygen, (b-3) Aluminium, (b-4) Silicon; (c) Size of matrix Al_2O_3 grain.

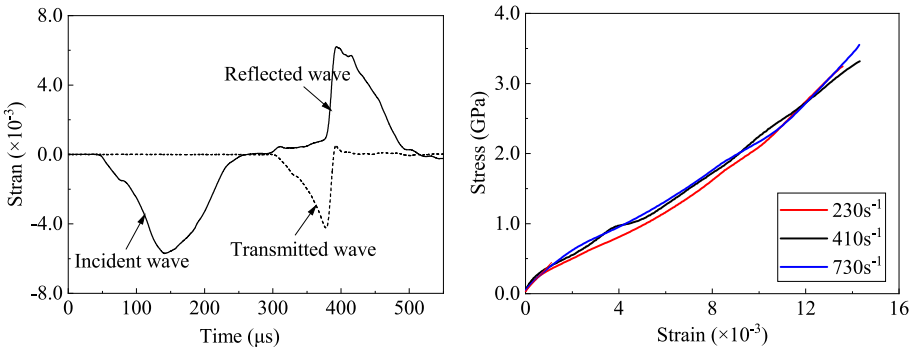

(a) Typical signal of SHPB tests (b) Stress-strain curves at different strain rates

Fig. 3. Compression mechanical properties of Al_2O_3/SiC composite.

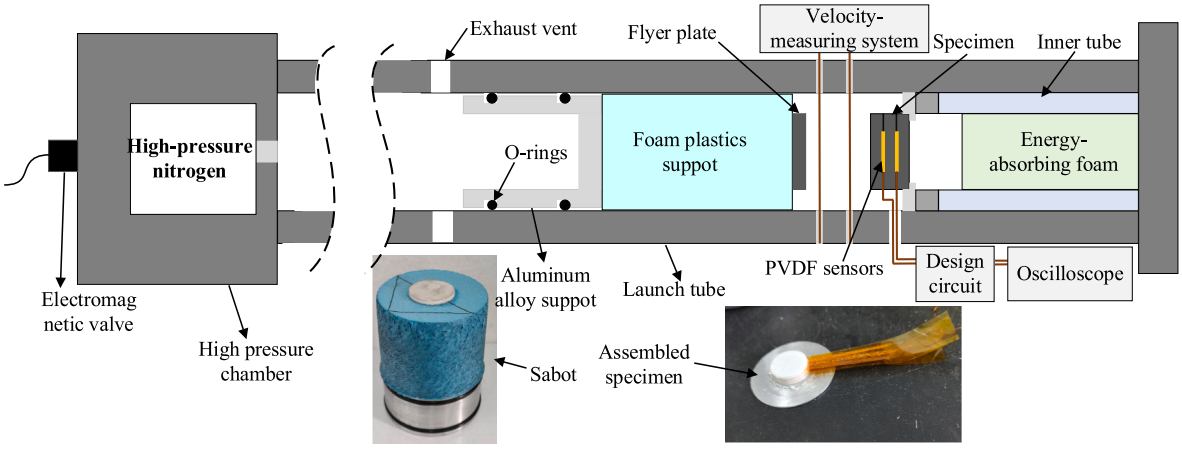

Fig. 4. Experimental design.

of 24 h. The polyvinylidene fluoride sensor (also called PVDF) exhibits high sensitivity to pressure. So, it was embedded between two layers of ceramic plates to capture the initiation and termination of the shock wave pulse. It's important to note that, due to the nonlinear characters of the calibration coefficient at higher pressure impacts, the pressure values measured by the PVDF sensors were considered only as reference values.

3. Results and discussion

3.1. Macroscopic shock response characteristic

According to the theory of the symmetrical impact, the particle velocity U_p is half of the impact velocity V of the flyer, expressed as $U_p = 0.5\ V$. The impact velocity was determined by the on–off signals of two fine copper wires corresponding to two channels (CH1 and CH2). The typical signal of the velocity-measuring system is shown in Fig. 5(a). The distance between the two wires is denoted as d_1, and the time taken for the flyer to pass through is Δt_1. Consequently, the impact velocity can be defined as $V = d_1/\Delta t_1$.

The shock wave velocity (U_s) was acquired using the PVDF testing system, and the characteristic signals are shown in Fig. 5(b). The shock wave is steady, which satisfied the assumption of Rankine Hugoniot equations. The predetermined distance (d_2) between two layers of PVDF sensors is 2 mm, and the time difference in the passage of the shock wave response is denoted as Δt_2. Consequently, the shock wave velocity can be

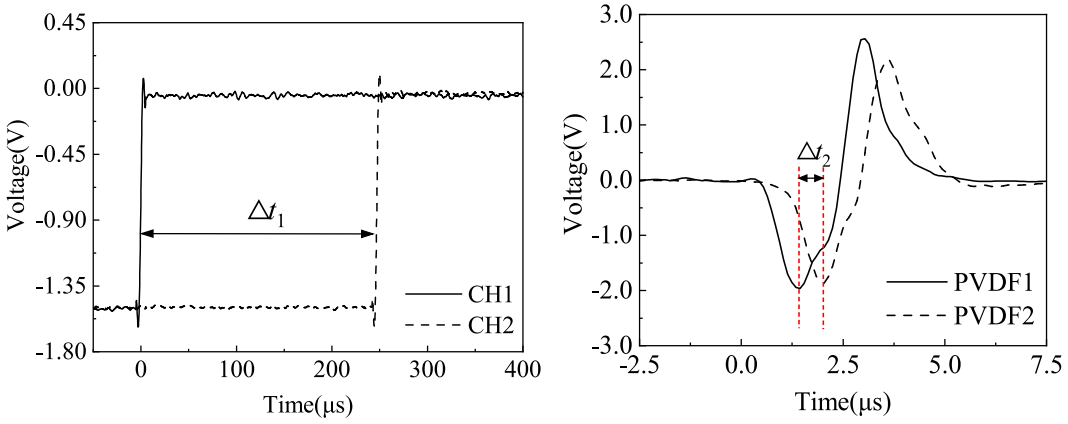

(a) Measuring of impact velocity (b) Signals of PVDF sensors

Fig. 5. Typical signals of experiments.

expressed as $U_s = d/\Delta t_2$. Finally, five valid experimental data were collected from the plane impact tests, and the results were presented in Table 1, where P is the hydrostatic pressure. The compressive volumetric strain can be described as $\mu = \rho/\rho_0$-1.

Based on steady Rankine-Hugoniot theory, the diagram of shock wave propagation is presented in Fig. 6. The coordinate frame is aligned with the shock wave, and the material moves from left to right. At the front of the shock wave, sharp discontinuities exist concerning pressure (P), density (ρ), and internal energy (E), denoted by the subscript 0 representing the state before the shock wave.

The steady Rankine-Hugoniot equation is derived from three conservation relations at the shock wave front: mass, momentum, and energy conservation, namely the Hugoniot shock adiabatic curve [35]. Previous studies have indicated that the relationship between shock wave velocity U_s and particle velocity U_p is linear for most condensed matter across a broad pressure range. The U_s-U_p relationship of the Al_2O_3/SiC composite, pure Al_2O_3 [36], and pure SiC [37] under the elastic stage was fitted by the least square method, as shown in Fig. 7(a). As shown, the equation of the state of the Al_2O_3/SiC composite is close to the pure polycrystals Al_2O_3.

When the ceramic material is intact, the P-μ Hugoniot curve can be expressed in polynomial form,

$$P = K_1\mu + K_2\mu^2 + K_3\mu^3 \quad (1)$$

For shock pressure lower than the *HEL*, K_1 can be described as $K + 4/3G$; K_2 and K_3 are constants. Parameters K and G represent bulk modulus and shear modulus respectively. The P-μ Hugoniot curve of the Al_2O_3/SiC composite was fitted by the least square method, as shown in 7(b).

3.2. Microscopic failure mechanism

In this study, second-phase SiC particles were not only distributed in the grain boundary of the matrix Al_2O_3 but also within the interior of the grain. The Al_2O_3/SiC composite can be considered as an intracrystalline/intergranular composite ceramic. In comparison with monocrystalline alumina, the addition of second-phase particles serves as a strengthening and toughening agent. To evaluate the micro fracture mode and damage mechanism of the Al_2O_3/SiC composite under different shock pressures, sample fragments were softly recovered in the plane impact experiments and analyzed using SEM techniques.

Table 1
Experimental results of flyer plate impact tests.

No.	V m/s	U_s m/s	U_p m/s	P GPa	μ
01	128	9880	64	2.32	0.0065
02	183	9905	94	3.33	0.0093
03	236	9920	118	4.29	0.0120
04	247	9930	124	4.51	0.0126
05	301	9980	150	5.51	0.0153

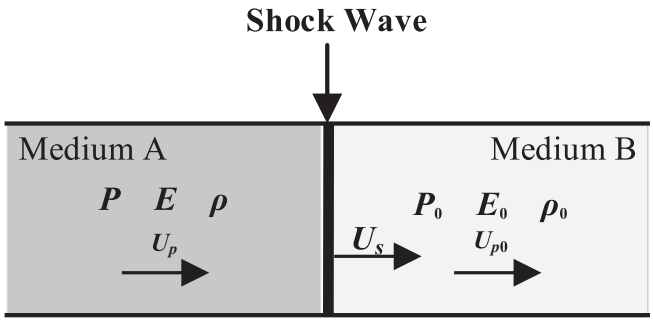

Fig. 6. Reference diagram for steady Rankine-Hugoniot equations.

Fig. 8 presents the SEM results of large fragments located at the edge of the sample and small fragments inside the specimen under low-impact pressure conditions (2.31GPa). In Fig. 8(a) and (b), numerous sharp edges and a few smooth fracture surfaces are observed in fragments at the edge of the sample, indicating the presence of both intergranular fractures (indicated by the red rectangular dotted line, labelled as "I") and transgranular fracture modes (labelled as "T"). The intergranular fracture predominates in the crack propagation. Fractured core areas (labelled as "H") are formed at the interfaces of multiple grains and initial defects. The fracture surface of the large fragments exhibits micro-cleavage fracture zones with river patterns and tongue shapes, marked as "C". Additionally, slip bands within the grains caused by shear slip are observed (labelled as "P"), along with local plastic deformation characteristics of single grains (labelled as "S") and the formation of grain boundary microcracks.

In Fig. 8(c) and (d), the small fragments within the specimen exhibit numerous smooth fracture surfaces (labelled as "T"), indicating that the predominant microfracture mode is transgranular fracture. Under the influence of in-plane shear stress, shear slip bands are observed on the fracture surface of single grains (labelled as "P"). In comparison to the fragments at the edge of the sample, local plastic deformation is evident around both the single grain and fractured core areas in the fragments inside the specimen.

Fig. 9 shows the SEM results of fragments under high impact pressure

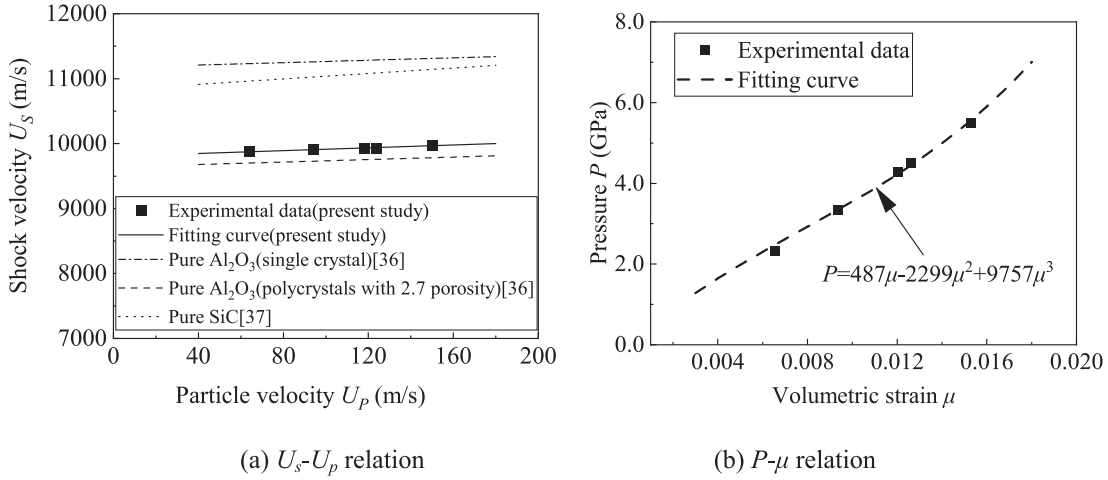

Fig. 7. Hugoniot curves of the Al_2O_3/SiC composite under plane shock loading.

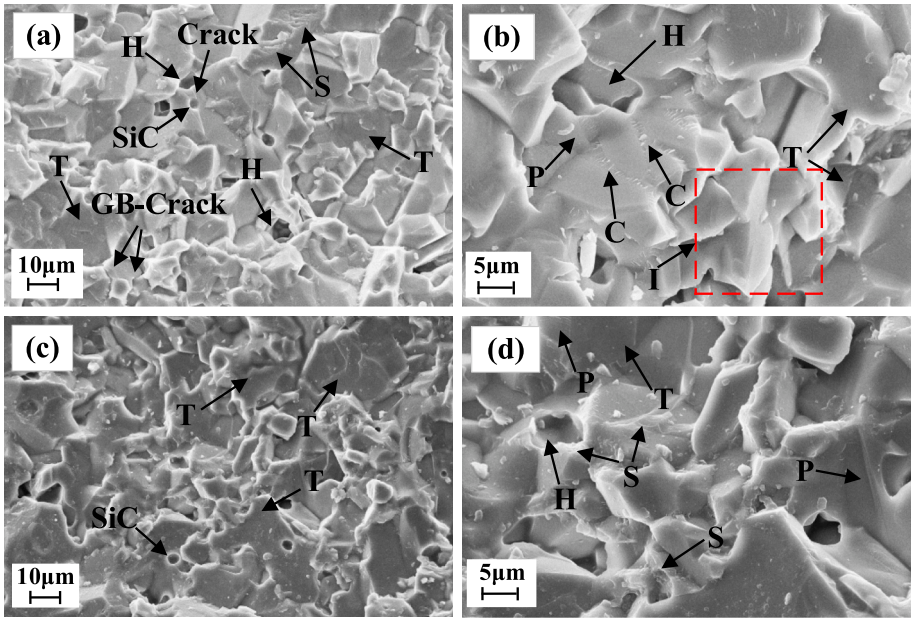

Fig. 8. Fracture surfaces of fragments under the impact pressure of 2.31GPa. (a) and (b) were the large fragments at the edge of the sample, (c) and (d) were the small fragments inside the specimen.

conditions (4.05GPa). In Fig. 9(a), the prevailing microfracture mode of the composite is transgranular fracture (labelled as "T"), with micro-cracks present at the grain boundary. On the section of a single grain, slip lines emerge due to shear stress, with the slip line being truncated at the grain boundary, forming a fractured core area (labelled P), as shown in Fig. 9(b). The grain surrounding the fractured core area exhibits local microplastic deformation (labelled as "S"). As seen in Fig. 9(c), in comparison to low impact pressure conditions, the characteristics of local microplastic deformation become more obvious, including micro-cleavage fractures (labelled as "C") and slip lines induced by shear stress. Numerous grains fracture, resulting in the formation of micro-cracks. In Fig. 9(d), the single grain displays both in-plane and out-of-plane shear deformation modes, along with a step-shaped microscopic cleavage area (indicated by the red oval dotted line, labelled as "S").

The macroscopic response of the Al_2O_3/SiC composite was significantly influenced by the microstructure of ceramic under impact compression loads, as observed through the analysis of microscopic fracture modes in fragments. Under low-pressure impact loading conditions, the predominant fracture mode in multi-phase ceramics is intergranular fracture. Micro-cracks appear at the matrix grain boundaries, along with cleavage fractures and micro-crack nucleation under local shear stress; however, large shear slip lines are notably absent. As the impact pressure increases, the microfracture mode of the multiphase ceramics gradually transitions to transgranular fracture. More shear-induced slip lines and micro-cleavage regions become evident, accompanied by pronounced local plastic deformation characteristics.

The presence of second-phase particles also influences the crack propagation and microfracture mode of the multiphase ceramics. In this study, second-phase particles are found either inside the matrix grains or anchored to the grain boundaries. Due to the mismatch in elastic modulus and thermal expansion coefficient between SiC particles and Al_2O_3 matrix grains, residual stress emerges between matrix grains and second-phase particles during the preparation of composite ceramics. During crack propagation, the second-phase particles become anchored to the grain boundary, leading to the deflection of microcracks and transgranular fracture, as shown in Fig. 10(a). Microcracks that deflect into the matrix grains result in the formation of more complex cracks near the second-phase particles, as shown in Fig. 10(b). When SiC

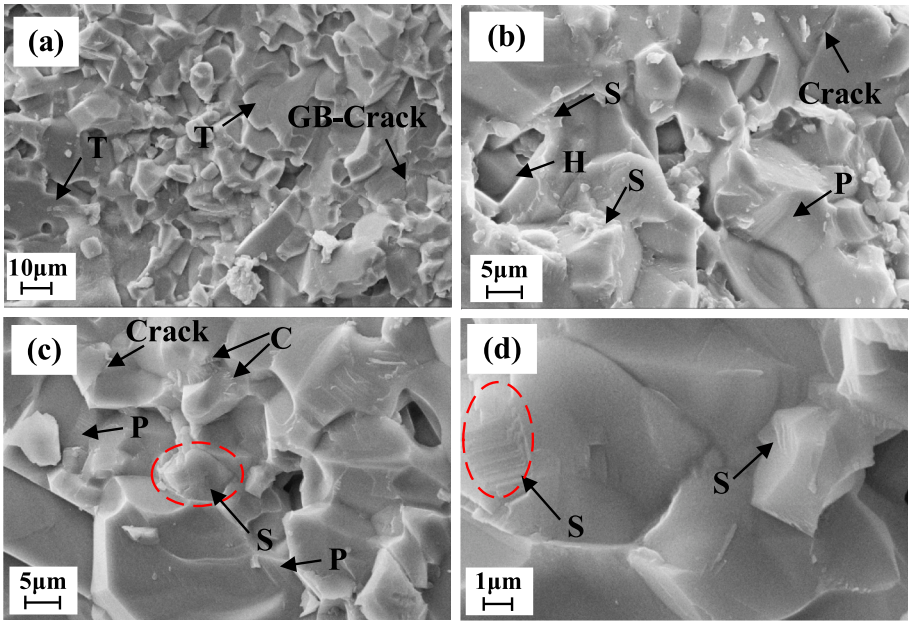

Fig. 9. Fracture surfaces of fragments inside the specimen under the impact pressure of 4.05GPa.

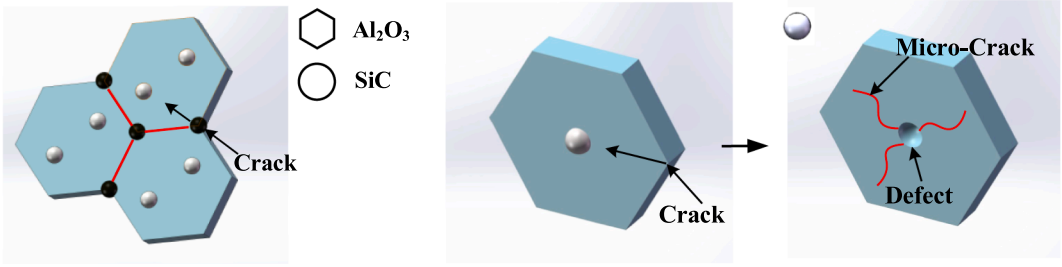

(a) Crack propagation mechanism (b) Formation of internal cracks in matrix grains

Fig. 10. Effect of SiC particles on crack propagation of composites.

particle is pulled out, microcracks and regions of micro-plastic deformation occur around the remaining defects, enhancing the propagation path of microcracks and improving the energy dissipation capacity of the composite ceramics. The microcracks at the interface between the second-phase particles and the matrix grains significantly impact the microfracture mode of the composite ceramics during the fracture process.

3.3. Distribution of fragments size under plane shock loading

3.3.1. Statistics of fragments

The size and shape of fragments play a crucial role in explaining the

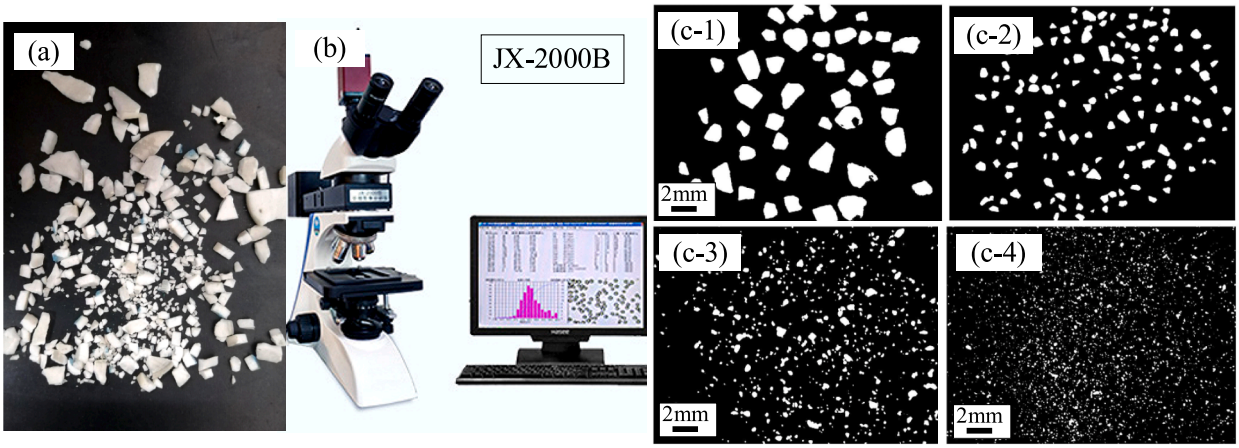

Fig. 11. Partial fragments of plane impact tests. (a) recovery fragments, (b) micro-image analyzer, (c) image binaryzation.

evolution of cracks and the release of energy. Under plane impact loading, Al_2O_3/SiC composite fractured into varying sizes and shapes fragments. Upon soft recovery of the sample, it is obvious that the sizes of fragments were uneven and diverse. Fragments in the middle of the sample were smaller, influenced by compression waves and spalling effects. Conversely, the fragments at the edge and sides of the sample were relatively larger, influenced by stress concentration and side sparse wave effects. The recycled particles were separated using an ultrasonic vibrator and sieving method. Then the images were processed through binarization. The Microimage Analyzer was employed to derive the particle size distribution, as shown in Fig. 11. In image analysis, the pixel serves as the smallest unit, each with a specific size. The diameter of a circle with the same area and the aspect ratio can be calculated by counting the number of pixels contained in each particle, and then the grain size distribution can be obtained by counting all the particles.

The particle size exhibited a wide distribution range under one-dimensional stress wave loading, categorized into five groups: minuscule particles (<300 μm), small-sized particles (300–500 μm), medium-sized particles (500–1000 μm), large-sized particles (1000–1500 μm), and super-sized particles (>1500 μm). The particle sizes were collected for statistical analysis, and the equivalent diameter was calculated using the Microimage Analyzer, as presented in Table 2. As shown, the specimen displayed the highest number of medium-sized particles at a low impact pressure of 2.32GPa. The count of minuscule particles increased with the increase in impact pressure.

In this study, the minimum impact pressure was 2.32GPa, which is below the dynamic compressive strength of multiphase ceramics. The tensile strength of the Al_2O_3/SiC composite is significantly lower than its compressive strength. The fracture was primarily induced by tensile stress during sparse wave propagation. When the flyer striked the plate specimen, left and right compression waves were generated at the contact interface. These waves reflected into sparse waves on the free surfaces, interacting to create a region of tensile stress, ultimately resulting in spalling of the specimen. Corresponding to the microfracture mode of the composite, under low impact pressure, more intergranular fractures led to the spallation of complete grains, resulting in larger size fragments. Conversely, under high impact pressure, the existence of transgranular fractures caused numerous grains to break up, producing finer fragments.

3.3.2. Previous typical models

(a) Grady model.

Grady [38] proposed a theoretical model for the fracture mechanism, based on the concept of inherent fracture-producing flaws and energy conservation. Within this model, the local kinetic energy T' of the fractured sphere element can be expressed as,

$$T' = \frac{2\pi}{45}\frac{\dot{\rho}^2}{\rho}S^5 \tag{2}$$

where S is the radius of sphere element, ρ is the density of material, $\dot{\rho}$ is the expanding density rate.

The total energy U can be described as,

$$U = \frac{3}{10}\frac{\dot{\rho}^2}{\rho A^2} + \gamma A \tag{3}$$

where γ is the energy associated with the creation of fragment surface area. A represents the fracture surface area density.

At the energy minimum, $dU/dA = 0$, and the equilibrium A can be expressed as,

$$A = (3\dot{\rho}^2/5\rho\gamma)^{1/3} \tag{4}$$

Assuming spherical or cubic fragments of equal size, the fragment diameter or size d is related to the surface area density $6/A$. For brittle fracture, the fracture energy is $K_{IC}^2/2\rho c_l^2$, and the strain rate is $\dot{\varepsilon} = \dot{\rho}/3\rho$, the nominal fragment size S can be described as,

$$S = \left(\frac{\sqrt{20}\,K_{IC}}{\rho c_l \dot{\varepsilon}}\right)^{2/3} \tag{5}$$

where c_l is the volume sound velocity.

(b) G&C model.

Glenn and Chudnovsky [39] modified Grady's fragmentation scale model by incorporating energy principles, presenting a revised theoretical model for fragmentation scale. The total available kinetic energy to fuel the breakage can be expressed in Eq. (2) too. As the brittle material undergoes uniform expansion, the strain energy of distortion becomes zero, and only the hydrostatic strain energy is considered. The assumption is made that fragments are stress-free upon their formation, allowing all stored elastic energy to be available for fragmentation. The surface energy associated with the fragments Γ_i can be simply expressed as,

$$4\pi N a^2 \gamma = \Gamma_i R/S \tag{6}$$

where R is the initial radius of the dilating body, N is expressed as $N=(R/a^3)$, a is the fragment radius.

The incremental surface energy $\Delta\Gamma$ acquired is,

$$-\Delta\Gamma = \Gamma_i(1 - R/S) \tag{7}$$

Balancing the change in energy of the system due to fragmentation,

$$\Delta T = \Delta P + \Delta\Gamma = T_i(a/R)^2 + P_i + \Gamma_i(1 - R/S) = 0 \tag{8}$$

$$S^3 + \alpha S - 2\beta = 0 \tag{9}$$

where $\alpha = \frac{3\sigma_c^2}{\rho E \dot{\varepsilon}_v^2}$; $\beta = \frac{2G_c}{2\rho\dot{\varepsilon}_v^2}$; E is the elastic modulus; σ_c is the fracture stress, which is identical to the local material strength at crack initiation; G_c is the fracture energy; $\dot{\varepsilon}_v$ is the linear expansion strain rate. T_i and P_i are the initial kinetic-energy and the stored elastic energy associated with the fragments respectively.

In general, the Eq. (9) can be simplified as,

$$S = 4\sqrt{\frac{\alpha}{3}}\sin\left(\frac{\phi}{3}\right) \tag{10}$$

$$\phi = \sinh^{-1}\beta(3/\alpha)^{3/2}$$

(c) DID model

Zhou et al. [17] introduced a kinetic model to predict the fragment size of brittle materials under dynamic loading, defined as the scale model based on the dynamics of isolated decohesion (DID model). The time interval t_f between crack nucleation and complete fracture can be

Table 2
Particle sizes of fractured ceramic at different impact pressure.

Particle size (μm)	Number of particles				
	2.32GPa	3.33GPa	4.29GPa	4.51GPa	5.51GPa
<300	1448	7683	13,151	13,791	15,073
300 ~ 500	2653	1670	6319	7050	6744
500 ~ 1000	415	303	236	272	210
1000 ~ 1500	192	141	264	188	162
>1500	90	256	322	210	86
Total number of particles	4798	10,053	20,292	21,511	22,275
Average diameter /μm	373	341	287	254	250

determined using the implicit analytic expression,

$$\left(\frac{\dot{\varepsilon}_v}{c\sigma_c^3/E^2G_c}\right)\left[\exp\left(\frac{ct_f}{EG_c/\sigma_c^2}\right)-\frac{ct_f}{EG_c/\sigma_c^2}-1\right]=1 \tag{13}$$

where c is the speed of elastic wave, $c=(E/\rho)^{1/2}$. In the fracture process, the crack propagation results in unloading in the neighbouring region. The single length of the unloading region is equal to ct_f.

Based on the DID hypothesis, the fragment size can be estimated as,

$$\exp(\overline{S}_{\mathrm{DID}})-\overline{S}_{\mathrm{DID}}-1=\overline{\dot{\varepsilon}}_v^{-1} \tag{14}$$

$$\overline{S}_{\mathrm{DID}}=\frac{s}{\bar{s}_0}=p_1\left[1+p_2\left(\frac{\dot{\varepsilon}_v}{\overline{\dot{\varepsilon}}_v}\right)^{p_3}+p_4\left(\frac{\dot{\varepsilon}_v}{\overline{\dot{\varepsilon}}_v}\right)^{p_5}\right]^{-1} \tag{15}$$

where $\bar{s}_0=\frac{EG_c}{\sigma_t^2}$, $\overline{\dot{\varepsilon}}_v=\frac{\dot{\varepsilon}_v}{\dot{\varepsilon}_{v0}}$, $\dot{\varepsilon}_v=\frac{c\sigma_c}{Eh}$, $\dot{\varepsilon}_{v0}=\frac{c\sigma_t^3}{E^2G_c}$; σ_t is tensile strength; p_1-p_5 are positive coefficients ($p_5>p_3$). Parameter p_1 represents the quasistatic limit of the normalized average fragment size. The two power terms of $p_2\left(\frac{\dot{\varepsilon}_v}{\dot{\varepsilon}_v}\right)^{p_3}$ and $p_4\left(\frac{\dot{\varepsilon}_v}{\dot{\varepsilon}_v}\right)^{p_5}$ correspond to the intermediate and highest strain-rate regimes respectively.

3.3.3. Modified model

In previous study, Gao et al. [2] conducted a one-dimensional stress dynamic compression test on the Al_2O_3/SiC composite. The particle-scale analysis of the recovered fragments was conducted based on the modified DID model. Results showed that recycled fragments were more agreed with the prediction of the modified DID model compared with the Grady model and G&C model [2].

However, the DID model is exclusively applicable for predicting the fragmentation size of brittle materials subjected to one-dimensional stress wave loading. Considering the material's application in the realm of armour protection, it is more likely to experience loading conditions characterized by extremely high strain rates, making it better suited for plane shock loading. In this case, the modulus should be modified as,

$$\widehat{E}=\frac{E}{1-\nu^2} \tag{16}$$

where ν is the Poisson's ratio.

The fracture energy is acquired as follows,

$$G_c=\frac{1}{\widehat{E}}K_{Ic}^2=\frac{1-\mu^2}{E}K_{Ic}^2 \tag{17}$$

where K_{Ic} is the fracture toughness of multiphase ceramics; $\overline{\dot{\varepsilon}}=\frac{\dot{\varepsilon}}{\dot{\varepsilon}_0}$, $\dot{\varepsilon}=\frac{c\sigma_c}{\widehat{E}h}$, $\dot{\varepsilon}_0=\frac{c\sigma_t^3}{\widehat{E}^2G_c}$, $\overline{S}_0=\frac{\widehat{E}G_c}{\sigma_t^2}$.

In Eq. (15), the $\dot{\varepsilon}_{v0}$ can be modified as,

$$\dot{\varepsilon}_{v0}=\frac{c\sigma_t^3}{E(1-\nu^2)K_{Ic}^2} \tag{18}$$

Based on the experimental data obtained from the plane impact experiments, the recovered sample fragments were subjected to theoretical analysis. The material parameters of the Al_2O_3/SiC composite and experimental data of the present study are detailed in Table 3 and Table 4 respectively.

The modified DID model presented in this paper will be compared with previous typical models. Firstly, the Grady model has undergone dimensionless processing, and can be simplified as,

Table 4
Experimental data of the present study.

No.	σ_c(GPa)	$\dot{\varepsilon}$(s^{-1})	$\dot{\varepsilon}/\dot{\varepsilon}_0$	Experimental data (Ave. particle size/mm)
01	2.32	6191	0.329	0.373
02	3.33	9287	0.494	0.341
03	4.29	12,342	0.657	0.287
04	4.51	12,986	0.691	0.254
05	5.51	16,282	0.866	0.250

$$\overline{S}_{\mathrm{Grady}}=\left[\frac{24}{(\overline{\dot{\varepsilon}})^2}\right]^{\frac{1}{3}} \tag{19}$$

The G&C model also needs to be modified. According to Eq. (15), the coefficient β can be expressed as,

$$\beta=\frac{2G_c}{2\rho\dot{\varepsilon}_v^2}=\frac{2(1+\nu^2)K_{Ic}^2}{2\rho\dot{\varepsilon}_v^2} \tag{20}$$

To make Eq. (10) dimensionless, the G&C model can be expressed as,

$$\overline{S}_{G\&C}=\frac{4}{\dot{\varepsilon}}\sinh\left[\frac{1}{3}\sinh^{-1}\left(\frac{3}{2}\overline{\dot{\varepsilon}}\right)\right] \tag{21}$$

The experimental data were subjected to fitting using the modified DID model,

$$\overline{S}_{\mathrm{ZHOU}}=\frac{s}{s_0}=4.5\left[1+0.77(\overline{\dot{\varepsilon}})^{\frac{1}{4}}+5.4(\overline{\dot{\varepsilon}})^{\frac{3}{4}}\right]^{-1} \tag{22}$$

Fig. 12 shows fragments scales under various plane impact pressures with the fitting results derived from three models. As shown, the dynamic fragment scale of the Al_2O_3/SiC composite aligns more closely with the modified DID model, although slightly exceeding the values predicted by the theoretical model. A notable difference exists between the predictive models for fragmentation scale based on energy conservation proposed by Grady, Glenn and Chudnovsky et al.

In Fig. 12, results indicate that considering only energy conservation under intense dynamic loading is insufficient. The initiation, propagation, and convergence of initial cracks in the material significantly

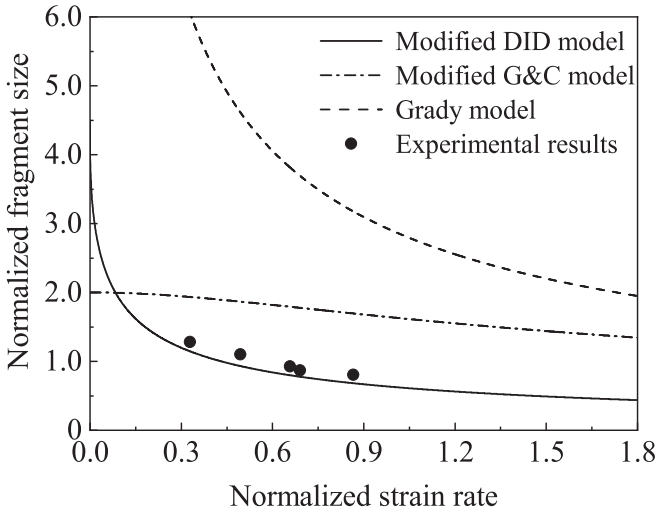

Fig. 12. Theoretical prediction of dynamic fragmentation scale.

Table 3
Mechanical properties parameters of the Al_2O_3/SiC composite.

ρ(g/cm^3)	E(GPa)	ν	c (m/s)	K_{Ic}(MPa·$m^{1/2}$)	G_c (N/m)	σ_t (MPa)	$\dot{\varepsilon}_0$(s^{-1})	$\bar{s}_0$
3.67	420	0.23	10,698	4.1	38	240	18,797	0.29

impact the prediction of the fragment size distribution. Influenced by the microstructure of the specimen, such as initial voids and microcracks, local stress concentration is easily generated, resulting in larger fragments observed in experiments. Microscopic structural analysis of the fracture surface reveals that under plane impact loading, the occurrence of local microscopic plastic deformation and the influence of second-phase particles make the propagation and expansion of cracks more complex. The presence of these factors causes the experimentally measured particle sizes to be larger than the predicted values of theoretical models.

4. Conclusions

This paper investigated the dynamic fracture behaviour and failure mechanisms of the Al_2O_3/SiC composite under plane shock loading through both experimental and theoretical analyses. The conclusions were drawn as follows.

(1) The Hugoniot curves of the Al_2O_3/SiC composite were obtained by a series of plate impact experiments, including U_s-U_p and P-μ relations.
(2) The SEM analysis was carried out to investigate the microfracture mechanisms of the Al_2O_3/SiC composite under different stress states, which consist of transgranular and intergranular fractures, microcracks, fractured core area, local plastic deformation, et al. Notably, local plastic deformation mainly occurred at the transgranular fracture of large grains and intergranular fracture of small grains.
(3) The second-phase SiC particles were found either inside the matrix grains or anchored to the grain boundaries. The particles influenced significantly on the crack propagation and microfracture mode of the Al_2O_3/SiC composite.
(4) After the soft recovery of specimens in impact experiments, a statistical analysis of ceramic fragments was conducted, and analytical models were developed and modified to predict the distribution of fragments under plane shock loading.

CRediT authorship contribution statement

Yubo Gao: Writing – review & editing, Writing – original draft, Project administration. **Zhihao Li:** Data curation. **Yanxin Ge:** Methodology, Formal analysis. **Liutong Shi:** Validation.

Declaration of competing interest

The authors declare that they have no known competing financial interests or personal relationships that could have appeared to influence the work reported in this paper.

Data availability

Data will be made available on request.

Acknowledgements

The research presented in this paper was carried out while Yubo Gao was serving as a visiting scholar at Nanyang Technological University of Singapore. The manuscript acknowledges financial support from the National Natural Science Foundation of China (grant number 12172337, 11702257), and the Foundation Research Program of Shanxi Province (No. 20210302123022), and the Science and Technology Innovation Project of Higher Education in Shanxi Province (No. 2019L0513).

References

[1] Y. Jiang, K. Qian, Y. Zhang, Y. Xia, Z. Xiong, Z. Zhang, K. Yu, Experimental characterisation and numerical simulation of ballistic penetration of columnar ceramic/fiber laminate composite armor, Mater. Des. 224 (2022) 111394.
[2] Y.B. Gao, Y.X. Ge, P. Xu, W. Zhang, X.M. Cai, J.J. Zhang, Dynamic fracture mechanism and fragmentation analysis of fine grained Al_2O_3/SiC composite, Mater. Sci. Eng. A 826 (2021) 141976.
[3] P.J. Hazell, G.J. Appleby-Thomas, S. Toone, Ballistic compaction of a confined ceramic powder by a non-deforming projectile: Experiments and simulations, Mater. Des. 56 (2014) 943–952.
[4] J. Lankford, The role of dynamic material properties in the performance of ceramic armor, Int. J. Appl. Ceram. Tec. 1 (2004) 205–210.
[5] I.E. Reimanis, A review of issues in the fracture of interfacial ceramics and ceramic composites, Mater. Sci. Eng. A 237 (1997) 159–167.
[6] J. Fu, K. Ren, L. Yin, R. Yang, T. Zhao, Z. Chen, Preparation methods and performance of new tungsten-based ceramic alloy, Mater. Des. 206 (2021) 109781.
[7] C.Y. Huang, Y.L. Chen, Design and impact resistant analysis of functionally graded Al_2O_3–ZrO_2 ceramic composite, Mater. Des. 91 (2016) 294–305.
[8] Y.B. Gao, T.G. Tang, C.H. Yi, W. Zhang, D.C. Li, W.B. Xie, W. Huang, N. Ye, Study of static and dynamic behavior of TiB_2–B_4C composite, Mater. Des. 92 (2016) 814–822.
[9] B.M.L. Koch, P. Jannotti, D. Mallick, B. Schuster, T. Sano, J.D. Hogan, Influence of microstructure on the impact failure of alumina, Mater. Sci. Eng. A 770 (2020) 138549.
[10] K.O. Pedersen, T. Brvik, O.S. Hopperstad, Fracture mechanisms of aluminium alloy AA7075-T651 under various loading conditions, Mater. Des. 32 (2011) 97–107.
[11] G. Wei, W. Zhang, Deformation and fracture behavior of steel projectiles impacting AD95 ceramic targets-experimental investigation, Journal of Physics: Conference Series, IOP Publishing 500 (2014) 182043.
[12] C. Denoual, F. Hild, A damage model for the dynamic fragmentation of brittle solids, Comput. Method. Appl. M. 183 (2000) 247–258.
[13] V.B. Shenoy, K.S. Kim, Disorder effects in dynamic fragmentation of brittle materials, J. Mech. Phys. Solids 51 (2003) 2023–2035.
[14] D.E. Grady, Fragment size distributions from the dynamic fragmentation of brittle solids, Int. J. Impact Eng. 35 (2008) 1557–1562.
[15] D.E. Grady, Length scales and size distributions in dynamic fragmentation, Int. J. Fracture 163 (2010) 85–99.
[16] W.J. Drugan, Dynamic fragmentation of brittle materials: analytical mechanics-based models, J. Mech. Phys. Solids 49 (2001) 1181–1208.
[17] F.H. Zhou, J.F. Molinari, K.T. Ramesh, Effects of material properties on the fragmentation of brittle materials, Int. J. Fracture 139 (2006) 169–196.
[18] F.H. Zhou, J.F. Molinari, K.T. Ramesh, Characteristic fragment size distributions in dynamic fragmentation, Appl. Phys. Lett. 88 (2006) 261918.
[19] Q.Y. Zhang, Y.X. Zheng, F.H. Zhou, T.X. Yu, Fragmentations of alumina(Al2O3) and silicon carbide(SiC) under quasi-static compression, Int. J. Mech. Sci. 167 (2020) 105119.
[20] S.B. Sapozhnikov, O.A. Kudryavtsev, N.Y. Dolganina, Experimental and numerical estimation of strength and fragmentation of different porosity alumina ceramics, Mater. Des. 88 (2015) 1042–1048.
[21] G.L. Hu, C.Q. Chen, K.T. Ramesh, J.W. McCauley, Mechanisms of dynamic deformation and dynamic failure in aluminum nitride, Acta Mater. 60 (2012) 3480–3490.
[22] M. Bhattacharya, S. Dalui, N. Dey, S. Bysakh, J. Ghosh, A.K. Mukhopadhyay, Low strain rate compressive failure mechanism of coarse grain alumina, Ceram. Int. 42 (2016) 9875–9886.
[23] Z.Y. Wang, P.F. Li, W.D. Song, Inelastic deformation micromechanism and modified fragmentation model for silicon carbide under dynamic compression, Mater. Des. 157 (2018) 244–250.
[24] A.K. Mukhopadhyay, K.D. Joshi, A. Dey, R. Chakraborty, A. Rav, S.K. Biswas, S. C. Gupta, Shock deformation of coarse grain alumina above Hugoniot elastic limit, J. Mater. Sci. 45 (2010) 3635–3651.
[25] G.R. Li, T. Suo, H.M. Wang, Y.T. Zhao, G. Chen, X.Z. Kai, Microstructure study of hot rolling nanosized in-situ Al_2O_3 particle reinforced A356 matrix composites, J. Alloy Compd. 855 (2021) 157107.
[26] N. Cherkasova, S. Veselov, A. Bataev, R. Kuzmin, N. Stukacheva, Structure and mechanical properties of ceramic materials based on alumina and zirconia with strontium hexaaluminate additives, Mater. Chem. Phys. 259 (2021) 123938.
[27] S.T. Alweendo, O.T. Johnson, B.M. Shongwe, F.P. Kavishe, J.O. Borode, Microstructural and mechanical properties of alumina (Al2O3) matrix composites reinforced with SiC from rice husk by spark plasma sintering, Mat. Res. 23 (2020) e20190363.
[28] K.S. Chandra, M. Monalisa, C.V.A. Chowdary, G. Ghosh, D. Sarkar, Microstructure and mechanical behaviour of SrO doped Al_2O_3 ceramics, Mater. Sci. Eng. A 739 (2019) 186–192.
[29] X.L. Shi, Y.L. Dong, F.M. Xu, Y. Tan, L. Wang, J.M. Yang, Preparation and properties of nano-SiC strengthening Al_2O_3 composite ceramics, Mater. Sci. Eng. A 528 (2011) 2246–2249.
[30] E. Gevorkyan, M. Rucki, S. Panchenko, D. Sofronov, L. Chalko, T. Mazur, Effect of SiC addition to Al_2O_3 ceramics used in cutting tools, Materials 13 (2020) 5195.
[31] Y.K. Jeong, K. Niihara, Microstructure and mechanical properties of pressureless sintered Al_2O_3/SiC nanocomposites, Nanostruct. Mater. 9 (1997) 193–196.
[32] Z.Y. Deng, J.L. Shi, Y.F. Zhang, Pinning effect of SiC particles on mechanical properties of Al_2O_3-SiC ceramic matrix composites, J. Eur. Ceram. Soc. 18 (1998) 501–508.

[33] D. Sciti, J. Vicens, A. Bellosi, Microstructure and mechanical properties of alumina-SiC nanocomposite prepared from ultrafine powders, J. Mater. Sci. 37 (2002) 3747–3758.
[34] Y.L. Dong, F.M. Xu, X.L. Shi, C. Zhang, Z.J. Zhang, J.M. Yang, Fabrication and mechanical properties of nano-/micro-sized Al_2O_3/SiC composites, Mater. Sci. Eng. A 504 (2009) 49–54.
[35] Y.B. Gao, C.H. Yi, W. Zhang, Y.J. Deng, Effect of TiB_2 on dynamic response of TiB_2-B_4C composites under shock wave loading, Int. J. Appl. Ceram. Tec. 16 (2019) 59–68.
[36] T. Mashimo, Y. Hanaoka, K. Nagayama, Elastoplastic properties under shock compression of Al_2O_3 single crystal and polycrystal, J. Appl. Phys. 63 (1988) 327–336.
[37] D.E. Grady, Dynamic properties of ceramic materials. Sandia National Lab. (SNL-NM), Albuquerque, NM (United States), 1995.
[38] D.E. Grady, M.E. Kipp, Mechanisms of dynamic fragmentation: factors governing fragment size, Mech. Mater. 4 (1985) 311–320.
[39] L.A. Glenn, A. Chudnovsky, Strain-energy effects on dynamic fragmentation, J. Appl. Phys. 59 (1986) 1379–1380.